PCCP

ROYAL SOCIETY OF CHEMISTRY

PAPER

View Article Online
View Journal | View Issue

Cite this: *Phys. Chem. Chem. Phys.*, 2024, **26**, 9284

Vertical growth of a 3D Ni–Co-LDH/N-doped graphene aerogel: a cost-effective and high-performance sulfur host for Li–S batteries†

Khalida Abaid Samawi,[a] Bassam A. Mohammed,[b] Ekhlas Abd-Alkuder Salman,[a] HassabAlla M. A. Mahmoud,[c] Aws Zuhair Sameen,[d] Sura Mohammad Mohealdeen,[e] G. Abdulkareem-Alsultan *[f] and Maadh Fawzi Nassar *[gh]

Sulfur hosts and conversion catalysts based on NiCo-LDHs exhibit potential for improving the performance of Li–S batteries. Nevertheless, their low electron conductivity and aggregation propensity restrict their applicability. This investigation employs a temporary scaffold of ZIF-67 to produce a nanotube assembly of Ni–Co-LDH encapsulated within an N-doped graphene sponge. The electrochemically developed interface has an extended active surface area, and the clumping of LDH nanosheets is effectively inhibited by the design of the nanotube arrangement. Furthermore, the incorporation of nitrogen within the structure of graphene results in a boost of electrical conductivity and provides an increased quantity of active sites. Interfacial electron transport is facilitated by the interfacial rearrangement of charges resulting from p–n heterojunctions and fosters redox activity. In this study, the researchers have presented the double role played by the nickel–cobalt layered double hydroxide (NiCo-LDH) nanotubes in improving the polysulphide (LiPS) conversion and decreasing the movement of the sulphur (S) ions by forming surface-bound intermediates. The battery that was fabricated using the above composite cathode mixture showed a higher energy storage ability, *i.e.*, 1190.0 mA h g^{-1} at J = 0.2. Furthermore, the battery showed a significantly higher capacity to rapidly supply energy and displayed a rate capacity of 670.1 mA h g^{-1} at J = 5C. Also, the above battery displayed a longer cycle life, with 1000 charge–discharge cycles and the deterioration rate of 0.029% for each cycle.

Received 24th November 2023,
Accepted 23rd February 2024

DOI: 10.1039/d3cp05716j

rsc.li/pccp

Introduction

In the past few years, there has been an increasing prevalence of electric vehicles and mobile devices, which has further increased the demand for fabricating high energy-density rechargeable batteries.[1] Out of the various eco-friendly energy conversion technologies, lithium–sulphur (Li–S) batteries are considered emerging alternatives for storing energy and have a theoretical energy density of 2600 W h kg^{-1} and a low environmental impact.[2] Furthermore, regarding commercial desirability, Li–S batteries outshine current lithium-ion batteries significantly. The remarkable qualities of sulfur, such as affordability and eco-friendliness, make Li–S batteries the top choice for many businesses. Not only do they offer better performance, but they also align with the growing demand for sustainable energy solutions. However, there are still significant obstacles to their widespread implementation. Sulfur has been known to have poor electrical conductivity, which poses a challenge in its usage. Additionally, a noticeable volume expansion occurs during the cycling process. A further challenge pertains to the electrochemical dissolution and transportation of the dissolved LiPS intermediates within the organic electrolyte. The above phenomenon is known as the shuttle effect, representing a significant obstacle encountered by high-efficiency

[a] *Department of Chemistry, College of Science, Al-Nahrain University, Baghdad, Iraq*
[b] *Thermal Mechanic Techniques Engineering Department, Basra Engineering Technical College, Southern Technical University, Basra, Iraq*
[c] *Department of Physics, Faculty of Sciences and Arts, King Khalid University, Muhayil Asir 63311, Saudi Arabia*
[d] *College of Medical Techniques, Al-Farahidi University, Baghdad, Iraq*
[e] *Department of Radiology & Sonar Techniques, Al-Noor University College, Nineveh, Iraq*
[f] *Faculty of Science and Natural Resources, Universiti Malaysia Sabah, 88400 Kota Kinabalu, Sabah, Malaysia. E-mail: kreem.alsultan@yahoo.com*
[g] *Integrated Chemical BioPhysics Research, Faculty of Science, Universiti Putra Malaysia, 43400 UPM Serdang, Selangor, Malaysia. E-mail: nassarmaadh@gmail.com*
[h] *Department of Chemistry, Faculty of Science, Universiti Putra Malaysia, 43400 UPM Serdang, Selangor, Malaysia*

† Electronic supplementary information (ESI) available. See DOI: https://doi.org/10.1039/d3cp05716j

lithium–sulfur (Li–S) batteries. This results in poor coulombic efficiency, fast self-discharge, and a marked decrease in the capacity of these batteries. Therefore, these concerns must be addressed for achieving effective and dependable results.[3,4]

Many researchers are working hard to lessen the shuttle effect and increase sulfur utilization to combat these limitations. The cathode's structure, electrolyte components, separator alterations, and lithium-metal anode durability have all been the subject of research.[5–8] Earlier studies have indicated that optimising the cathode structure is important to improve the functioning of the processes related to the electrochemical reactions involved in Li–S batteries. Several studies have addressed the issues related to volume expansion and poor electrical conductivity presented by sulphur (S) ions, wherein the researchers have assessed different carbon (C)-based materials displaying conductive properties, such as graphene, mesoporous C, and C nanotubes, as the probable hosts for S.[9–15] In this study, the researchers have aimed to control the volumetric fluctuations and improve the electrical conductivity of the cathodes. To mitigate the LiPS shuttle phenomenon, various polar components, including heteroatom-doped carbon, metal oxides, sulfides, carbides, metal hydroxides, and polymers, have been incorporated into the cathodes. These materials possess a strong affinity for LiPSs, effectively suppressing the dissolution of LiPSs within the cathodes. Consequently, this approach significantly enhances the cycling efficiency of the electrodes.[16–21] Furthermore, it has been found that the synergic effects of adsorption and electrocatalytic capabilities significantly impede the dissolution of polysulfides and effectively reduce the shuttle effect.[22]

There is a growing consensus that layered double hydroxides (LDHs) are the promising choice for this purpose. LDHs are highly desired hosts for sulfur because of their distinctive two-dimensional (2D) layered structure consisting of layers with positive charges and interlayer anions. They have an amazing capacity for chemical adsorption and rapid redox reaction.[23] The variability of the structure and composition of LDHs allows for precise control over their morphology, crystalline structures, interlayer anions, and electronic structures. Moreover, plentiful hydrophilic and hydroxyl groups have been found to be influential factors in enhancing reaction kinetics, thanks to their capability to link chemically with LiPSs. The following are the primary structural characteristics of LDHs: (i) exfoliating single-layer nanosheets of LDHs, each with a thickness of 0.48 nm, and constructing them into thin films is a simple process. Because of this, they can act as an impediment and stop the shuttle of polysulfides. The wholly exposed surface areas of individual LDH nanosheets also display unique benefits, which facilitate the transformation of polysulfides and lithium deposition.[24–26] (ii) Through the use of an *in situ* growth process, LDHs are capable of being easily shaped into a wide variety of nanoarchitectures, such as nanoflowers, extremely fine nanosheet arrays, and core–shell nanowire arrays.[23,27] (iii) These nanoarchitectures enable LDHs to be implemented as S hosts, which promote the process rate and improve polysulfide confinement capability because of their distinctive buffer area, abundant channels, and wide surface area. Using topotactic transition procedures, LDHs can be converted into a wide variety of transition metal-based substances (such as metal sulfides, phosphides, and nitrides) and two-dimensional carbons.[7,28] Additionally, the surface chemical composition of LDHs can be modified through cationic doping or the introduction of metal and oxygen deficiencies inside the LDH host sheets. These findings contribute to discovering additional reaction spots and enhancing the electrochemical performance of LDHs. The beneficial effects of LDHs provide an assurance of their outstanding applications in Li–S batteries.

Several reports have highlighted the significant role of LDHs as sulfur host materials in Li–S batteries. Recently, Chen *et al.* fabricated NiAl-LDH fences covered on H_3PO_4-activated BC (PAB) as an effectual sulfur host.[23] In another work, an innovative spongy NiFe-LDH polyhedron was synthesized by Zhang *et al.* and used as the sulfur host to improve the cathode electrode's efficacy.[29] The volume growth of sulfur is accommodated by the spongy structure of the NiFe-LDH polyhedron, which also supplies adequate spots for the adsorption of polysulfides. Additionally, Lu *et al.* have proven the ability of NiCo-LDH to function as a combinatorial facilitator in the suppression of polysulfides, effectively inhibiting the diffusion of polysulfides and accelerating the transformation of polysulfides. The NiCo-LDH shells were grown directly on S molecules and subsequently combined with a GO/CNT hybrid in their study.[30]

Although LDH-based nanomaterials have made notable advancements in Li–S batteries, it is important to recognize that this area of research is still in its early stage and significant obstacles need to be addressed. Firstly, optimising the architectural layout and streamlining the fabrication method are necessary. Secondly, precise insights are required to elucidate the underlying mechanism and the kinetic alterations occurring during the reaction process, which will contribute to the advancement of rational design strategies to achieve optimal structural characteristics and desirable chemical properties.

In this study, we successfully synthesized a unique structure consisting of 3D Ni–Co layered double hydroxide nanotube arrays (Ni–Co-LDH NTA) that were grown *in situ* on a hierarchical framework of N-doped graphene sponge (NGS) structures. This framework is referred to as 3D Ni–Co-LDH NTA/NGS. In particular, the 3D N-doped graphene sponge was created from a colloidal solution of graphene oxide employing a straightforward freeze-drying approach; it is ideally suited for use as a basal growth medium due to its significant porosity, large specific surface area, and swift electrical and ionic conductivities. A complete and persuasive investigation examined the relationship between the hybrid structure and the improvement in electrochemical performance. The incorporation of nitrogen-doped carbon nanosheets with improved conductivity in a 3D heterostructure, along with vertical LDH nanotube arrays, presents a multitude of advantages: (1) the fabricated cathode displayed a significant physical and chemical affinity for the S species, which could effectively decrease the shuttle effect; (2) it was noted that the cathode showed a higher

electronic conductivity, wherein the charge transport paths were reduced and the redox reactions of LiPSs were expedited due to the reaction sites of the layered double hydroxide (LDH) that were attached to the C structure. It was noted that the porous C structure could efficiently tolerate the volume expansion of S ions and ensure a higher loading capacity for S ions. Therefore, using a 3D Ni–Co-LDH NTA/NGS electrode in a Li–S battery allows for large areal capacity, excellent rate efficiency, and an extended battery life.

Experimental

Preparation of an N-doped graphene oxide sponge

The modified version of Hummers' method was utilized to oxidize the natural graphite. The graphite oxide (GO) was dissolved in deionized water at a concentration of 6 mg mL^{-1} and subsequently mixed with a 20 mL solution containing melamine using ultrasonic blending for two hours. The mass proportion of melamine to GO was 1 : 4.[31] The resulting NGO hydrogel was used in the subsequent steps.

Preparation of NiCo LDH nanotubes

NiCo-LDH nanotubes have been fabricated *via* the template method reported in the literature.[32] The implementation of the following procedures resulted in the successful preparation of the NiCo LDH nanotubes. Initially, a dispersion of MoO_3 nanorods, fabricated based on the previously reported hydrothermal method,[33] was prepared by adding 60 mg of the nanorods to 80 mL of methanol solvent. Subsequently, three supplementary components were incorporated into the solution. Inclusion of 0.7 g of $Ni(NO_3)\cdot 6H_2O$ ($Co(NO_3)\cdot 6H_2O$), 0.9 g of 2-methylimidazole, and 1.2 g of polyvinyl pyrrolidone (PVP) was performed. Subsequently, the solution was agitated under ambient conditions for 5 hours, following which the MoO_3@ZIF-67 composite was separated by filtration. The solution vigorously stirred at room temperature for five hours before MoO_3@ZIF-67 was passed through a filter. The resulting MoO_3@ZIF-67 composite was subsequently mixed in 50 mL of methanol, accompanied by 50 mg of $Ni(NO_3)_2$, and reacted at 90 °C for four hours to convert it to MoO_3@NiCo LDH. Following that, the MoO_3 in MoO_3@NiCo LDH was washed away with an NH_3H_2O solution (2 M), and NiCo LDH nanotubes were produced.

Preparation of the 3D NiCo LDH nanotube/NGS heterostructure

20 mg of prepared NiCo LDH nanotubes and 50 mg of NGS were dispersed in a mixture of DI water and ethanol (50%/%50 v/v). The mixture was placed in a Teflon-lined hydrothermal reactor and heated at 90 degree Celsius for 4 hours. Finally, the obtained solution with viscous dispersion underwent freeze-drying for one day using a lyophilizer, resulting in the 3D Ni–Co-LDH NTA/NGS structure (Scheme 1).

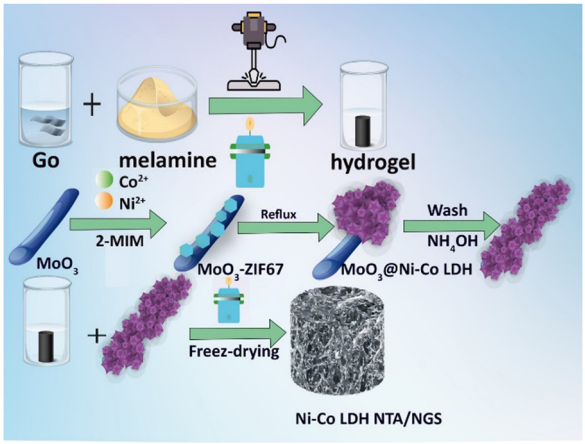

Scheme 1 Illustration of the Ni–Co-LDH NTA/NGS preparation process.

Preparation of Ni–Co-LDH NTA/NGS/S, Ni–Co-LDH NTA/S, and NGS/S

The drying process of the sulfur powder was conducted at a precise temperature of 40 °C for six hours. Subsequently, the powder was thoroughly ground with the prepared composite at a mass ratio of 3 : 1 (Ni–Co-LDH NTA/NGS/S). The cathode material was prepared by heating the powder at 160 °C in an argon atmosphere for 8 hours. The sample was subjected to further heating at 255 °C for 45 minutes to remove excess sulfur from the surface, followed by a reduction to room temperature. The resulting cathode material was combined with sulfur. Ni–Co-LDH NTA/S and NGS/S were prepared using the same method as above, with a fixed mixture of sublimated sulfur at a ratio of 2 : 1.

Materials characterization

The structures and morphologies of the fabricated composites were investigated using transmission electron microscopy (TEM), field emission scanning electron microscopy (FESEM), and high-resolution TEM (HRTEM). Furthermore, the results of the X-ray diffraction (XRD) process indicated the presence of phase transitions and crystalline structures in the samples. The surface composition was determined by X-ray photoelectron spectroscopy (XPS) at ambient temperature. The NGS and S concentrations in the Ni–Co-LDH-NTA/NGS/S mixture were determined using a thermogravimetric analyser. The results showed that all diffraction peaks in the H-NiCo-LDH structure were shifted and broadened, which could be probably due to the development of a homogenous shell and the concurrent etching of the sacrificial template, wherein the two processes increased the residual strain.

Cell assembly

Asymmetric cells. Conductive modifiers (10 wt% Super-P and 10 wt% PVDF) were mixed with the fabricated cathode composite in a solution of nitromethyl pyrrolidone at a weight-to-weight ratio of 8 : 1 : 1. After stirring for 24 hours, the liquid was deposited onto an aluminum collector. The thickness of

the layer ranged from 100 to 120 μm. It was allowed to dry at 48 °C and then sliced into spherical electrode sheets with an outer diameter of 12 mm. The cathode showed an S loading of ≈1.5 mg cm^{-2}. In this study, the researchers developed a high-loading cathode by thermally treating the S and Super C composite (in a 7 : 2 ratio) at 156 °C for 12 h. The composition of the slurry was altered to 90% S/Super C composite and 10% LA133. The slurry base mixture was composed of *n*-propanol and DI H_2O (in a 3 : 1 mass ratio). The electrode was then filled with 6 mg cm^{-2} S. The *E*/*S* ratio was decreased to 6 in the batteries having a high S load. The anode electrode was constructed using a flawless Li metal that was separated by two layers of polypropylene (PP). The electrolyte was formed by mixing 1,2-dimethoxyethane and 1,3-dioxolane (v/v; 1 : 1) with 1 wt% $LiNO_3$ (lithium nitrate) and 1 M Li bis (trifluoromethanesulfonyl)imide (LiTFSI). The electrolyte to S ratio was set at 40, indicated as E/S = 40. The addition of $LiNO_3$ to the electrolyte shields the Li anode from damage, while hindering the movement of soluble Li–LiPSs. The electrolyte was incorporated at a rate of 10 L mg^{-1} S, alternating between the positive and negative terminals two times. CR 2032 cells were assembled in the argon (Ar)-saturated glovebox. The researchers conducted cyclic voltammetry (CV) experiments using the Metrohm® Autolab® electrochemical analyzer at different scan rates. The Metrohm® Autolab® frequency analyzer was used to conduct electrochemical impedance spectroscopy (EIS) experiments, wherein the measurements were conducted at the frequency values ranging between 0.01 and 105 Hz.

Li_2S_6 symmetric cells

The mass proportion of Ni–Co-LDH NTA/NGS to the PVDF binder in the mixture was 90 : 10. A carbon-coated aluminium sheet was used to make the combined slurry. After drying under vacuum at 65 °C for 12 hours, the sheet was sliced into discs 10 mm in diameter. Using a PP membrane as a separator and an Li_2S_6-based electrolyte, a standard CR2025 battery was constructed with two analogous electrodes. In addition, the electrolyte had trace amounts of LiTFSI (1 mol L^{-1}) and $LiNO_3$ (1% w/w). In order to determine the CV of symmetric cells, the voltage was scanned at a speed of 10 mV s^{-1} from a voltage of −1.0 V to 1.0 V.

Adsorption experiment

The adsorption experiment was performed in a glass vessel that contained both Ar gas and a solution of Li_2S_6 with a concentration of 1 M. After introducing sulfur and Li_2S at a mole proportion of 6 : 1 into the combined solvent of 1,2-dimethoxyethane (DME) and 1,3-dioxolane (DOL) with an identical ratio of volume, the Li_2S_6 solution was created by vigorously stirring the mixture at a temperature of 60 °C.

Results and discussion

TEM and HRTEM characterized the microstructures of fabricated samples, as shown in Fig. 1. The freeze-dried 3D NGS has

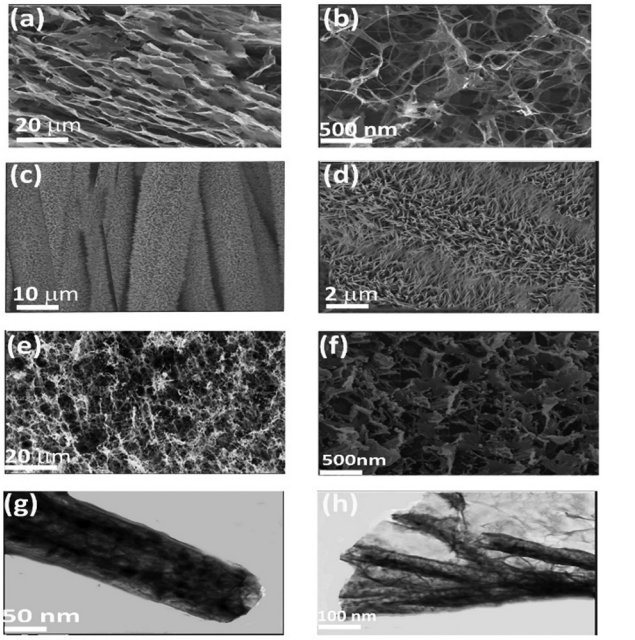

Fig. 1 SEM images of (a), (b) NGS in different directions, (c), (d) Ni–Co-LDH NTA, and (e), (f) Ni–Co-LDH NTA/NGS and TEM images of (g) Ni–Co-LDH NTA and (h) Ni–Co-LDH NTA/NGS.

a clearly defined and interlinked 3D porous structure (Fig. 1(a) and (b)), making it look like a sponge. The pore walls of the NGS consist of exceptionally thin layers of stacked graphene sheets. Fig. 1(c) and (d) display the vertical morphology of Ni–Co-LDH NTA formed on NGS nanosheets. The SEM images, depicted in Fig. 1(e) and (f), indicate that using Ni–Co-LDH nanotubes effectively inhibits graphene nanosheet agglomeration. The use of TEM enabled the thorough examination of the morphology growth and in-depth structural properties of Ni–Co-LDH NTA/NGS. Fig. 1(g) and (h) show the characteristic TEM images of Ni–Co-LDH NTA nanotubes, revealing a verified diameter of around 100 nm and a rough wall thickness of about 20 nm. An additional electron microscopy analysis was conducted in order to unveil the structure of Ni–Co LDH NTA/GNS/S. The magnified SEM image reveals many swollen structures, with the diameter ranging from 10 to 20 nm, on the surface of the Ni–Co LDH NTA/GNS layer (Fig. S1, ESI†). Fig. S1b (ESI†) shows a typical SAED pattern looking down the Ni–Co LDH NTA/GNS/S face, derived from the TEM analysis. Based on the measured *d*-spacings, the diffraction rings can be used to identify sulphur crystals or takovite-type structures. The measured spacings (0.115, 0.125, and 0.150 nm) match the pattern expected for a specific type of Ni–Co LDH crystal. Other spacings (0.205 and 0.242 nm) match the pattern expected for sulfur nanocrystals. EDX (Fig. S2, ESI†) elemental mapping of the Ni–Co LDH NTA/GNS/S particles reveals that Ni, Co, N, C, and S are distributed uniformly.

X-ray diffraction (XRD) experiments were conducted in order to examine the compositions and phase structures of Ni–Co-LDH NTA/NGS, Ni–Co-LDH NTA, and NGS (Fig. 2(a)). The diffraction peaks observed at angles of 25° and 42° could be

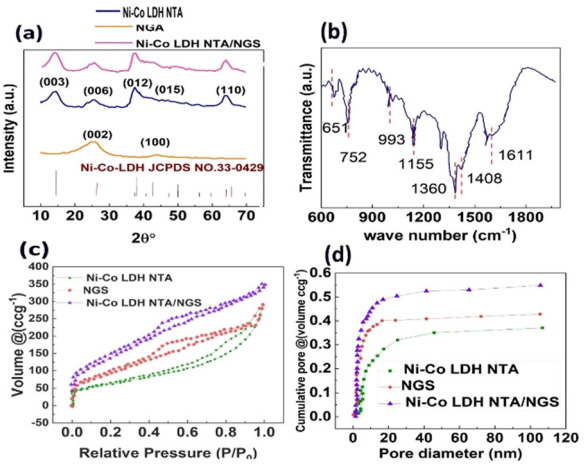

Fig. 2 (a) XRD patterns of Ni–Co-LDH NTA/NGS, Ni–Co-LDH NTA and NGS, (b) FTIR spectra of Ni–Co-LDH NTA/NGS, (c) nitrogen adsorption–desorption isotherms, and (d) the pore size distribution of Ni–Co-LDH NTA/NGS, Ni–Co-LDH NTA, and NGS.

ascribed to the (0 0 2) and (1 0 0) crystallographic planes of NGS, respectively.[34,35] The observed peaks at angles of 14.7, 25.5, 36.9, 42.1, and 63.8°, which are related to (0 0 3), (0 0 6), (0 1 2), (0 1 5), and (1 1 0) crystalline planes, exhibit a strong correlation with the hexagonal crystal structure of NiCo-LDH (JCPDS no. 33-0429).[36] It has been observed that the diffraction peaks of Ni–Co-LDH notably broaden along with the changes in peak position; this is likely attributable to the development of a homogeneous shell and the simultaneous engraving of a sacrificial template, both of which lead to increased residual strain.[37,38]

The FTIR spectra of the as-synthesised compounds were analysed to identify their functional groups (Fig. 2(b)). The band found at 1611 cm^{-1} corresponds to the bending vibrational mode of H_2O molecules that have been adsorbed by the hydrogen (H) bonds.[39] The signal at 1408 cm^{-1} was attributable to the O–H functional group in NGS. Also, the spectral peaks noted at the 1155 and 993 cm^{-1} wavelengths were ascribed to the C–O stretching vibration. The bands noted in the short wavelength range of 600–800 cm^{-1} originated from the stretching vibrations of the Ni–O and Co, Ni–OH, and Co–OH bonds observed in the NiCo-LDH compound.[40,41]

The distribution of the pore diameters and the particular surface area of the cathode compound show a significant impact on S confinement and conversion in Li–S batteries. Earlier studies have indicated that the electrolyte ion transfer is enhanced by a large specific surface area, a suitable pore size distribution and a significant number of easily available mesopores. The nitrogen (N) adsorption/desorption isotherms were used to evaluate the pore structures of the as-prepared compound structures. As depicted in Fig. 2(b), the isotherm of GA shows a remarkable increase in adsorption in a relative pressure range of 0.9 to 1.0, which can be attributed to a significant quantity of textural macropores. In the case of NGS, pores with a size less than 25 nm constituted just 45% of the overall volume (Fig. 2(c)). Conversely, pores smaller than 25 nm contributed to approximately 91% of the entire pore volume. This observation suggests that the introduction of Ni–Co-LDH NTA has resulted in the formation of a significant amount of finer mesopores. The calculated surface areas of the three fabricated structures are 400, 450, and 600 $m^2\ g^{-1}$. Notably, the Ni–Co-LDH NTA/NGS sample demonstrates the greatest specific surface area, measuring 600 $m^2\ g^{-1}$. This value is comparable to that of the reported graphene aerogel.[42]

Furthermore, the pore volume of the Ni–Co-LDH NTA/NGS composite is 0.55 $cm^3\ g^{-1}$, which is also higher than the pore volumes of Ni–Co-LDH NTA (0.12 $cm^3\ g^{-1}$) and NGS (0.09 $cm^3\ g^{-1}$). Consequently, the inclusion of Ni–Co-LDH NTA has resulted in alterations in the distribution of pore sizes and the specific surface area, thereby facilitating enhanced ion adsorption. The Ni–Co-LDH nanotubes are intercalated among the graphene layers to act as spacers. This arrangement leads to the separation of additional graphene sheets, forming more mesopores and resulting in an increased specific surface area.

The researchers used the XPS technique for analysing the elemental ratio and chemical properties of NiCo-LDH-NTA/NGS. The analysis of the NiCo-LDH-NTA/NGS XPS spectra (Fig. 3(a)) revealed the below elemental levels for C, N, O, Ni, and Co, *i.e.*, 38.2, 6.4, 41.5, 9.7, and 4.2, respectively. The EDS analysis showed that the levels of Co and Ni ions were equivalent to C and N levels, indicating that NiCo-LDH develops homogeneously on the NGS surface (Fig. S4, ESI†). As shown in Fig. 3(b), the C1s spectra could be categorised into three peaks at 284.5, 286.4, and 288.8 eV, which corresponded to the below-mentioned bonds: C=C/C–C, C–O, and C=O.[43,44] Furthermore, it was seen that the addition of nitrogen into

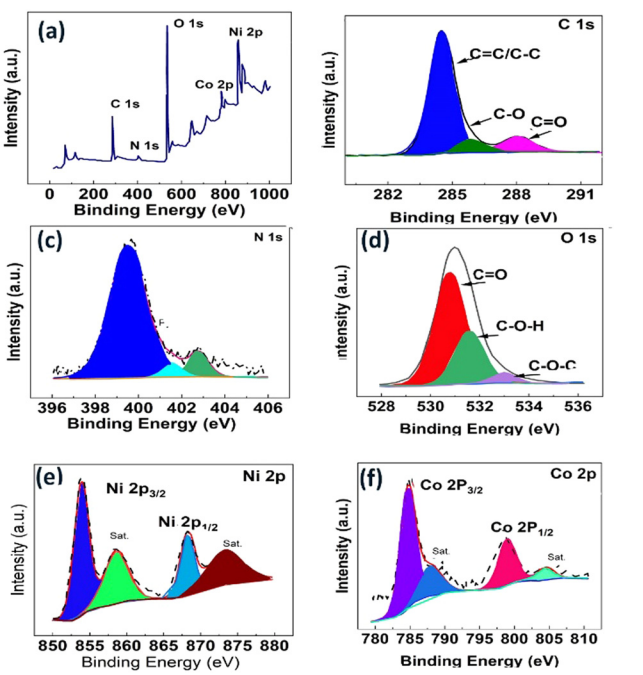

Fig. 3 (a) XPS survey spectrogram of Ni–Co-LDH NTA/NGS and high-resolution deconvoluted XPS spectra of (b) C 1s, (c) N 1s, (d) O 1s, (e) Ni 2p and (f) Co 2p of Ni–Co-LDH NTA/NGS.

the C structure increased the free charges and provided a large number of active sites. The high-resolution spectra of the N1s band (Fig. 3(c)) were deconvoluted into three peaks at 399.8, 401.5, and 402.6 eV. These peaks were found to be related to pyrrolic N, graphitic N, and oxidised N, respectively.[45,46] Furthermore, the O1s spectra (Fig. 3(d)) were categorised into three different peaks, which represented the C═O, C–OH, and C–O–C bonds at 530.5, 531.5, and 533.0 eV, respectively. Fig. 2(e) presents the Ni 2p spectrum. In this figure, the visible peaks corresponded to Ni $2p_{3/2}$ (854.9 eV) and Ni $2p_{1/2}$ (872.6 eV). These peaks are indicative of the presence of Ni^{2+} ions and are known as spin–orbit doublets, which are a characteristic feature of this type of analysis. Additionally, two prominent satellite signals are observed at 857.5 eV and 874.8 eV.[47,48] Correspondingly, the Co 2p spectrum (shown in Fig. 3(f)) reveals two prominent peaks at energy levels of 784.5 eV and 798.0 eV. These specific peaks correspond to the Co $2p_{3/2}$ and Co $2p_{1/2}$ spin–orbit doublets of Co^{2+}, respectively.[49]

The thermogravimetric technique was used to determine the sulfur percentages of the samples. The sulfur mass percentages of Ni–Co-LDH NTA/NGS/S, Ni–Co-LDH NTA/S, and NGS/S, when using a sulfur/host substance mass ratio of 4 : 1, are 78.9%, 77.8%, and 77.2%, respectively. It is noteworthy that Ni–Co-LDH NTA/NGS exhibits a marginally elevated evaporation temperature of sulfur when compared to NGS and Ni–Co-LDH NTA/S. The observed increase can be attributed to the enhanced confinement ability of the existing polar Ni–Co-LDH NTA/NGS towards sulfur, as illustrated in Fig. S5 (ESI†).

Adsorption

Conducting an adsorption test and analyzing its results were imperative to comprehend the process of polysulfide adsorption by LDHs and justify the exceptional efficiency of Ni–Co-LDH NTA/NGS compared to Ni–Co-LDH NTA and NGS. The adsorption investigation was conducted, and the resultant supernatant was afterwards analyzed using UV-vis spectroscopy. Additionally, XPS was performed on the solid material retrieved from the solution. The digital photographs, shown in Fig. 4(a), were captured subsequent to a 12-hour period of maintaining a static state. There is a discernible visual distinction observed among those four glass bottles. The solution containing Li_2S_6 exhibits a strong yellow hue, while the solution containing the Ni–Co-LDH NTA/NGS host becomes completely uncoloured upon adsorption. This indicates the exceptional adsorption activity of the Ni–Co-LDH NTA/NGS host towards Li_2S_6. The concentration variation of Li_2S_6 in the resulting solution was additionally measured using UV-vis spectroscopy (Fig. 4(b)). The absorption peak of Li_2S_6 in the liquid phase of the Ni–Co-LDH NTA/NGS/Li_2S_6 solution exhibits a lower intensity in comparison with those of the Ni–Co-LDH NTA/Li_2S_6 and NGS/Li_2S_6 solutions. This finding provides further confirmation that Ni–Co-LDH NTA/NGS/Li_2S_6 possesses a greater ability than Ni–Co-LDH NTA/Li_2S_6 to effectively attach to lithium polysulfides and mitigate the back and forth sulfur transition throughout the discharge/charge processes. The information obtained from the XPS experiment can shed further insight into

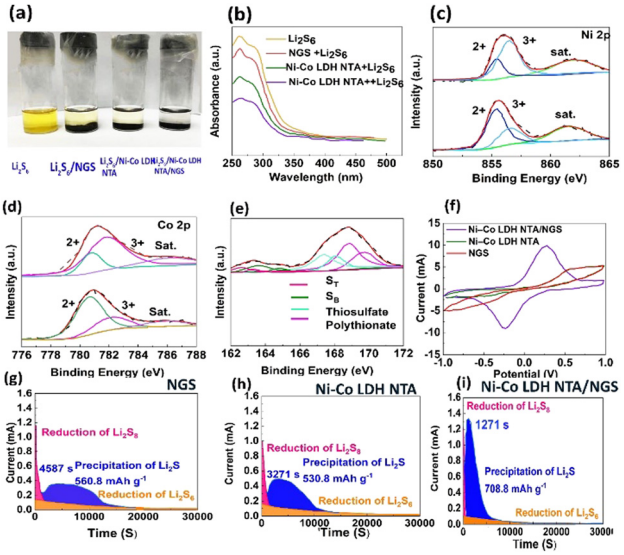

Fig. 4 (a) Digital photo of the adsorption experiment, (b) UV-vis spectra of pristine Li_2S_6, Ni–Co-LDH NTA/NGS/Li_2S_6, Ni–Co-LDH NTA/Li_2S_6, NGS/Li_2S_6, (c), (d) high-resolution XPS spectra of Co2p and Ni 2P of Ni–Co-LDH NTA/NGS and Ni–Co-LDH NTA/NGS/Li_2S_6, (e) high-resolution XPS spectra of S 2p of Ni–Co-LDH NTA/NGS/Li_2S_6, (f) CV curves of the symmetric cell Ni–Co-LDH NTA/NGS at 0.1 mV s^{-1} from 1.9 to 4.0 V (*vs.* Li^+/Li), and potentiostatic discharge curves of (g) NGS, (h) Ni–Co-LDH NTA, and (i) Ni–Co-LDH NTA/NGS.

the underlying process of the interaction of polysulfides with fabricated composites. As can be seen in Fig. 4(c), the emergence of Ni^{3+} peak in the Ni $2p_{3/2}$ spectrum of Ni–Co-LDH NTA/NGS/Li_2S_6 is due to the aforementioned chemical interaction with sulfur. Fig. 4(c) shows that Ni^{3+} on the surface was reduced to Ni^{2+} after exposure to Li_2S_6, and analogous behavior is seen in the Co $2p_{3/2}$ spectrum (Fig. 4(d)). The S 2p spectra (Fig. 4(e)) of Ni–Co-LDH NTA/NGS/Li_2S_6 have two fitted peaks at 162.0 and 163.9 eV, which are attributed to the presence of ''terminal'' (S_T) and ''linker'' sulfur (S_B) originating from LiPSs, respectively.[50] The peaks observed at binding energies ranging from 166 to 172 eV exhibit higher strength and can be effectively characterized by two distinct sulfur components. The peaks observed at 168.1 and 168.4 eV in the fitting analysis are attributed to surface-bound thiosulfate. The peaks observed result from the oxidation reactions of sulfur components that come from polysulfides.[51] The 169.1 and 170.1 eV peaks indicate that the polythionate structure is generated by an interaction between anchoring thiosulfate and polysulfides.[52] As a result, the polythionate complex forms when polysulfides are inserted into the SS bond of thiosulfate. By converting the dissolved polysulfides (Li_2S_x, $x < 4$) into more insoluble mediators, polythionate architecture and short-chain polysulfides (Li_2S_y, $y < 3$), the negative impact of the shuttle effect is greatly minimized. This process effectively traps the polysulfides, resulting in improved performance.

In order to conduct a more comprehensive examination of the influence of fabricated composites on the redox kinetics of LiPSs, the three prepared composites are employed as the electrode components in a symmetric cell. The cell is subjected

to CV experiments, with Li_2S_6 solution serving as the electrolyte. Fig. 4(e) demonstrates that Ni–Co-LDH NTA/NGS exhibits the highest current density among the materials investigated for the battery. This indicates that Ni–Co-LDH NTA/NGS possesses superior catalytic properties for converting LiPSs and exhibits exceptional redox kinetics in the domain of lithium–sulfur (Li–S) batteries. Following the galvanic discharge of the cells, the Li_2S deposition procedure was initiated with application of a constant potential of 2.05 V. Fig. 4(g)–(i) illustrate the dynamic decreasing current curves for the cells constructed utilizing different electrodes.

In theory, the complete process of transforming Li_2S_4 into Li_2S may supply more than 75% of sulfur's overall capacity.[53] As a result, a procedure that assists in the precipitation of Li_2S could be necessary for increasing the capacity and rate efficiency of Li–S batteries. When conducting the potentiostatic nucleation test, we used Li_2S_8 solution as the catholyte. This allowed us to investigate how the Ni–Co-LDH NTA/NGS particles affected the liquid-to-solid conversion reaction. However, the conversion of dissolved Li_2S_4 particles in the liquid phase into solid-phase Li_2S is a long process, which contributes to the low efficiency of the overall process. It has been found that after a constant decrease in current throughout the early stage, a distinctive peak would develop, which can be ascribed to the electrochemical deposition of Li_2S.[54] It is interesting to note that the deposition capacities of Li_2S on the NGS and Ni–Co-LDH NTA electrodes in Fig. 4(g) and (h) are quite similar, with values of 530.8 mA h g^{-1} for NGS and 561.8 mA h g^{-1} for Ni–Co-LDH NTA. However, it appears that Ni–Co-LDH NTA, which does not have 'triple-phase' sites within the electrode, achieves peak current more quickly than the NGS sample, as per Faraday's law. The cell that contains the Ni–Co-LDH NTA/NGS electrode reaches its peak current with the maximum capacity of 708.8 mA h g^{-1} for Li_2S in only 1271 seconds (Fig. 4(f)). In the meantime, the nucleation peaks of Li_2S on the Ni–Co-LDH NTA/NGS electrode are noticeably more distinct in comparison to those of Li_2S on the NGS and Ni–Co-LDH NTA electrodes. These results suggest that the kinetics of conversion from LiPS to Li_2S for the Ni–Co-LDH NTA/NGS host particles have been significantly enhanced.

To further verify the sulfur redox process (Fig. 5(a)), CV curves of Ni–Co-LDH NTA/NGS/S, Ni–Co-LDH NTA/S, and NGS/S cathodes are plotted. The presence of two reduction peaks at 2.29 V and 2.053 V for Ni–Co-LDH NTA/NGS/S indicates that S_8 is first converted to long-chain lithium sulfide species (Li_2S_x, $4 < x < 8$) and subsequently to short-chain Li_2S_2/Li_2S. The inversion of the Li_2S_2/Li_2S conversion to S_8 is responsible for the 2.4 V oxidation peak that is observed.[55] The maximum current response is observed at the Ni–Co-LDH NTA/NGS/S cathode despite the fact that it is somewhat more polarized than the NGS/S cathode. While it is possible that Ni–Co-LDH's polarity might reduce the electrode's electrical conductivity, this would mean that more sulfur-rich entities could participate in the reaction, which would boost the utilization rate of active components.[56] At 0.2C, the charge/discharge curves of Ni–Co-LDH NTA/NGS/S, Ni–Co-LDH NTA/S, and NGS/S cathodes

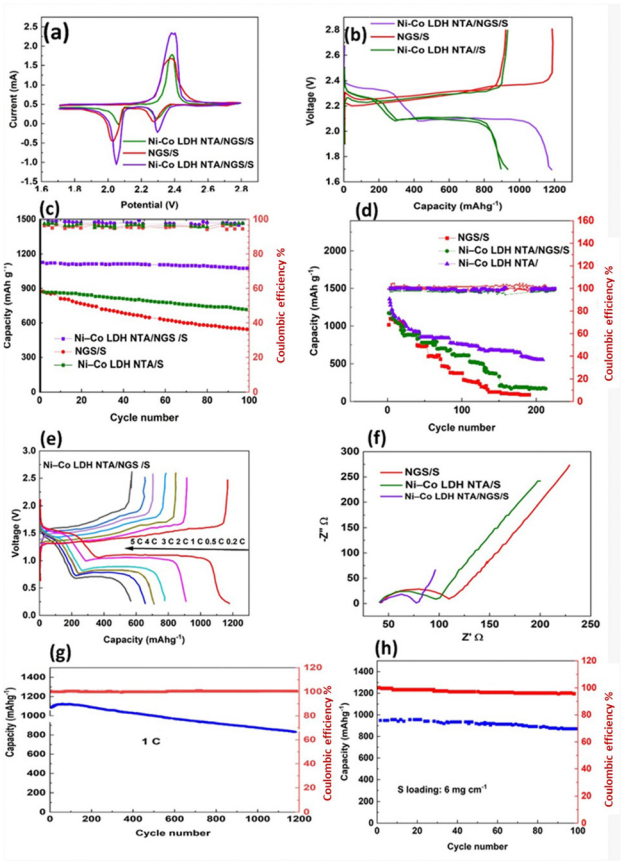

Fig. 5 Electrochemical characteristics of Ni–Co-LDH NTA/NGS/S, Ni–Co-LDH NTA/S, and NGS/S cathodes: (a) cyclic voltammogram at 0.1 mV s^{-1}. (b) Charging and discharging plots at 0.2C; (c) cycling performance at 0.2C; (d) rate performance; (e) charging and discharging plots of Ni–Co-LDH NTA/NGS/S at various current densities; (f) electrochemical impedance curves; (g) cycling stability of the Ni–Co-LDH NTA/NGS/S cathode at 1C; and (h) cycling performance of the Ni–Co-LDH NTA/NGS/S cathode with a sulphur loading of 6 mg cm^{-2} at 0.2C.

exhibit two plateaus for the discharge current and one plateau for the charge current, respectively. This is inferred from the matching outcomes of the CV plots. The voltage (ΔE) variation observed between the charge and discharge plateaus represents the process rates associated with the electrochemical reaction.

The polarization voltage observed in the Ni–Co-LDH NTA/NGS/S electrode (ΔE = 153 mV) is comparatively lower than that observed in the NGS/S cathode (ΔE = 195 mV) and the Ni–Co-LDH NTA/S cathode (ΔE = 235 mV). This discrepancy suggests the enhanced redox kinetics and recharging ability of the Li–S batteries (Fig. 5(b)).

In order to compare the electrochemical performances of Ni–Co-LDH NTA/NGS, Ni-LDH NTA/NGS and Co-LDH NTA/NGS, the cyclic voltammogram at 0.1 mV s^{-1} is obtained. Charging and discharging plots at 0.2C are obtained and displayed in Fig. S6 (ESI†). As can be inferred from Fig. S6 (ESI†) Ni–Co-LDH NTA/NGS shows a higher catalytic activity toward LiPS conversion than Ni-LDH NTA/NGS and Co-LDH NTA/NGS.

The cycle durability of the various electrodes is additionally assessed at a rate of 0.2C, as depicted in Fig. 5(c). The Ni–Co-LDH NTA/NGS/S electrode shows a starting discharge capacity of 1190 mA h g^{-1}, which is subsequently maintained at 1143 mA h g^{-1} after 100 cycles, indicating a capacity retention of 95%. The Ni–Co-LDH NTA/NGS/S cathode exhibits superior cycling stability and the highest coulombic efficiency compared to the other two samples. The remarkable cycle stability seen for Ni–Co-LDH NTA/S can be attributed to the synergistic impact of polar LDH and N-doped three-dimensional porous graphene. This combination enhances its adsorption and catalytic properties towards lithium polysulfides (LiPSs), effectively suppressing the shuttle effect.

Fig. 5(d) illustrates the Ni–Co-LDH NTA/NGS/S composite's rated capacity, demonstrating its enhanced performance. The discharge capacity values at various rates are as follows: 1190 (at 0.3C), 912.9 (at 0.6C), 850.2 (at 1C), 780.7 (at 2C), 708.2 (at 3C), 653.9 (at 4C), and 570.1 (at 5C) mA h g^{-1}. Upon the abrupt transition of the current density to 0.2C, the specific capacity of the Ni–Co-LDH NTA/NGS/S cathode exhibits an immediate recovery to 910.6 mA h g^{-1}. This restoration is accompanied by a capacity retention rate of 78%, which is evidence of the cathode's outstanding durability and capability to maintain its substantial reversibility during fast cycling. Conversely, the NGS/S cathode and the Ni–Co-LDH NTA/NGS/S cathode display the first discharge capacities of 1060.9 and 820.0 mA h g^{-1}, respectively, under demanding current densities. These values are lower than the discharge capacity of the Ni–Co-LDH NTA/NGS/S cathode. In addition, the charge–discharge curves of the Ni–Co-LDH NTA/NGS/S cathode, as shown in Fig. 5(e), demonstrate distinct dual plateaus even when subjected to a high current density of 5C. This observation indicates the rapid transformation kinetics of LiPSs.

EIS is conducted to facilitate the subsequent analysis of redox kinetics, as depicted in Fig. 5(f). The point of intersection between the arcs within the high-frequency area corresponds to the contact resistance (R_s). The arc observed in the center and high-frequency areas of the impedance spectrum can be attributed to the interfacial charge transfer resistance (R_{ct}). On the other hand, the sloped lines observed in the low-frequency zones are accountable for the Warburg diffusion impedance (Z_W). Table S1 (ESI†) summarizes the fitted electrochemical parameters for R_s and R_{ct}. When compared with the cathodes of Ni–Co-LDH NTA/S and NGS/S, it is observed that the Ni–Co-LDH NTA/NGS/S cathode exhibits a smaller charge transport resistance. This suggests that the Ni–Co-LDH NTA/NGS/S cathode has a fast charge transfer capacity, enabling the rapid transformation of LiPSs.

The NiCo-LDH-NTA/NGS/S cathode shows an initial discharge capacity of 929.5 mA h g^{-1}, which slowly decreases to 630.4 mA h g^{-1} after 1000 cycles. A high coulombic efficiency (CE) leads to a low-capacity depletion rate of 0.029% for every cycle. The NiCo-LDH-NTA/NGS/S cathode exhibits exceptional cycling stability, as evidenced by a low-capacity degradation rate of 0.029% in each cycle and a high average CE of 99.8%. The findings show that the NiCo-LDH-NTA/NGS/S composite displays a high cycling stability. The NiCo-LDH-NTA/NGS/S cathode, which is characterised by the S loading of 6 mg cm^{-2}, has an initial specific capacity of 943.3 mA h g^{-1} at the rate of 0.2C. After 110 cycles, the battery exhibits a reversible capacity of 823.3 mA h g^{-1} (Fig. 5(h)). Furthermore, the reported cathodes exhibit impressive cycling stability, as demonstrated by a low-capacity degradation rate of 0.11% per cycle, in addition to a significant CE.

To provide a more comprehensive explanation for the enhanced cycling performance, the DFT calculations were employed to examine the interaction between LiPSs and NiCo-LDH. A strong binding impact is indicated by the distortion of the geometric structure of polysulfides after they are trapped by the LDH nanoflakes (Fig. S7a, ESI†). The general consensus is that a higher binding strength is preferable. The LDH nanoflakes cause a significant distortion in the geometric structure of polysulfides, as seen in Fig. S7a (ESI†), suggesting a noticeable binding effect. The formation of ionic bonds between the Li atoms (in Li_2S_n) and the O atoms (in the LDH) in our system was evident from the charge density difference (Fig. S7b, ESI†). This is due to the total electron loss surrounding the Li atoms and the gross electron transfer between the Li atoms and their nearby O atoms in the LDH. Following adsorption of Li_2S_n, the O atoms experience a boost of approximately 0.6 *e*, as determined by Bader charge analysis; therefore, the Li atoms send charges to the O atoms (Fig. S7c, ESI†). According to previous work by Zhang *et al.*,[57] the chemical bonding between Li atoms in Li_2S_n groups and S (or O) atoms in 2D crystals is the root cause of the bonding between Li_2S_n groups and 2D materials (Fig. S7d, ESI†).

In addition, the electrochemical nature of the LDH/NGS interface was investigated. Nitrogen doping in graphene breaks the Π-conjugated system and changes the electrical structure. Material electron concentration rises as nitrogen atoms give lone electrons. A higher electron concentration in n-doped graphene moves the Fermi level closer to the conduction band than in pristine graphene. Thus, electron conduction is easier, making the material an n-type semiconductor.[58,59] The n-type behavior of n-doped graphene can be confirmed by measuring conductivity (n- or p-type) using Hall effect measurements.[60] Hall effect measurements were conducted on nitrogen-doped reduced graphene oxide (NGS) samples at a temperature of 300 K. These measurements were performed to analyze the electrical conductivity, charge carrier mobility, and carrier type. The results of the measurements are presented in Table S2 (ESI†). The increased electrical conductivity of the NGS samples can be attributed to the further reduction of graphene oxide, an increase in sp^2-related domains, and the presence of nitrogen doping. Moreover, the XPS study demonstrated that the prevailing feature of NGS samples was the pyrrolic-N bonding configuration. Through this configuration, the Stone–Wales effect is mitigated, while electron conduction pathways are created in carbon atoms. Consequently, n-type electrical conductivity enhanced, eliminating the conduction gap.

In order to evaluate the optical bandgaps of NGS and Ni–Co-LDH NTA samples, UV/vis was implemented. The UV/vis

absorption spectra of an NGS thin film that has been deposited on a glass substrate are shown in Fig. S8a (ESI†). The equation $\alpha h\nu = A(h\nu - E_g)^n$ is utilized in the Tauc-plot to depict the bandgap energies of several materials (Fig. S8 band c, ESI†). By applying Mott–Schottky plot analysis, the valence band edge and potential of the conduction band edge in the Ni–Co-LDH NTA and NGS samples have been calculated. Approximately, the estimated flat-band potentials of Ni–Co-LDH NTA and NGS were +1.63 V and −1.39 V against Ag/AgCl, respectively, Fig. S8(d) and (e) (ESI†). This estimate was based on extrapolating the observed negative and positive slopes of the curve, which represent the p-type and n-type semiconducting behaviours of NiCo-LDH-NTA and NGS, respectively. This is calculated using the following equation: $E_{RHE} = E_{Ag/AgCl} + 0.197 + 0.059$ pH. The Fermi energy level is approximately 0.10 eV lower than the minimal energy levels of the conduction band (C_B) and higher than the maximal energy levels of the valence band (V_B) for the n-type and p-type semiconductors, respectively.[61] Consequently, the position of the C_B and V_B edges was established by subtracting the energy gap (E_g) from the energy of the V_B (E_{VB}), as indicated in the scheme, in conjunction with the optical band gap energy acquired from UV-visible DRS data. Additionally, the Mott–Schottky curve of the NGS exhibited an inverted V-shape pattern, providing confirmation of the presence of a p–n junction contact between Ni–Co-LDH NTA and NGS. This can be viewed in Fig. S8(f) (ESI†). Following the completion of electron transfer and the formation of a stable p–n heterojunction, the buildup of electrons on NGS enhances the reduction activity, whereas the development of holes on Ni–Co-LDH improves the oxidation activity. Thus, the internal electric field produced by the p–n junction facilitates the redistribution of interfacial charges, thereby promoting the transfer of electrons at the interface and increasing the redox activity.

Conclusions

In brief, the Ni–Co-LDH NTA/NGS composite was synthesized as the sulfur host through the hydrothermal method. The outstanding behavior of the host can be ascribed to the following factors: the Ni–Co-LDH NTA/NGS/S composite possesses a porous structure that offers a significant specific surface area, along with a multitude of active sites. These characteristics enable it to effectively handle the expanding volume of sulfur, particularly when subjected to heavy sulfur loading. (2) The simultaneous introduction of nitrogen (N) additionally enhances the electrical conductivity of electrons and the capacity for adsorption of lithium polysulfides (LiPSs). Ni–Co-LDH exhibits strong polar characteristics, enabling it to adsorb lithium polysulfides (LiPSs) efficiently due to its chemical adsorption capability. This adsorption process facilitates the redox conversion reaction of LiPSs, thus mitigating the shuttle effect. Based on the findings mentioned above, it can be concluded that the Ni–Co-LDH NTA/NGS/S composite demonstrates exceptional performance over an extended period of cycling, as evidenced by a capacity decline ratio of 0.029% per cycle after undergoing 1000 cycles at a rate of 1C. The specific capacity of the Ni–Co-LDH NTA/NGS/S composite may achieve a value of 823.3 mA h g^{-1} even when subjected to a high sulfur loading of 6 mg cm^{-2}. This performance is seen after 110 cycles at a rate of 0.2C.

Data availability

The ESI† contains detailed information about synthesis, sample preparation and data supporting the findings of this study.

Author contributions

Khalida Abaid Samawi: resources; Bassam A. Mohammed: investigation; Ekhlas Abd-Alkuder Salman: funding acquisition; HassabAlla M. A. Mahmoud & Aws Zuhair: methodology, investigation; G. Abdulkareem-Alsultan & Sura Mohammad: reviewing and editing; and Maadh Fawzi Nassar: methodology, investigation, conceptualization, validation, writing – original draft, writing – reviewing and editing.

Conflicts of interest

There are no conflicts to declare.

Acknowledgements

The authors extend their appreciation to the Deanship of Scientific Research at King Khalid University for funding this work through large group Research Project under grant number RGP2/281/44.

Notes and references

1 M. Faraji, S. Yousefzadeh, M. F. Nassar and M. M. A. Zahra, *J. Alloys Compd.*, 2022, **927**, 167115.
2 H. Zhang, L. Yang, P. Zhang, C. Lu, D. Sha, B. Yan, W. He, M. Zhou, W. Zhang, L. Pan and Z. Sun, *Adv. Mater.*, 2021, **33**(21), 2008447.
3 C. Zhao, F. Ge, L. Shi, H. Wang, J. Liu, J. Zhang, S. Hou, H. Yu and C. Hu, *Int. J. Hydrogen Energy*, 2019, **44**, 30478–30485.
4 H. Raza, S. Bai, J. Cheng, S. Majumder, H. Zhu, Q. Liu, G. Zheng, X. Li and G. Chen, *Electrochem. Energy Rev.*, 2023, **6**, 29.
5 Y. Q. Wang, Y. S. Zhao, X. X. Yang, M. X. Ren, B. Y. Lei, W. J. Meng and D. L. Zhao, *Int. J. Hydrogen Energy*, 2020, **45**, 32654–32663.
6 K. Shi, Y. Lin, J. Li, Z. Xiong, J. Liao and Q. Liu, *Int. J. Hydrogen Energy*, 2022, **47**, 21662–21672.
7 J. Duan, Y. Zou, Z. Li, B. Long and Y. Du, *J. Electroanal. Chem.*, 2019, **847**, 113187.
8 G. Cao, R. Duan and X. Li, *Energy Chem.*, 2023, **5**, 100096.

9 F. Y. Fan, W. C. Carter and Y.-M. Chiang, *Adv. Mater.*, 2015, **27**, 5203–5209.
10 J. Ren, Y. Zhou, M. Guo, Q. Zheng and D. Lin, *Int. J. Hydrogen Energy*, 2018, **43**, 20022–20032.
11 R. Jiang, M. Jiang, Z. Huang, J. Wang, Y. Kuang and C. Fu, *Int. J. Hydrogen Energy*, 2020, **45**, 14940–14952.
12 K. Samawi, E. Salman, H. Hasan, H. Mahmoud, S. M. Mohealdeen, A. G. Alsultan, E. A. Malek and M. Nassar, *Mol. Syst. Des. Eng.*, 2024, DOI: **10.1039/D3ME00191A**.
13 L. Chen, H. Zhou, C. Fu, Z. Chen, C. Xu and Y. Kuang, *Int. J. Hydrogen Energy*, 2016, **41**, 21850–21860.
14 X. Qian, Y. Wang, L. Jin, J. Cheng, J. Chen and B. Huang, *J. Electroanal. Chem.*, 2022, **907**, 116029.
15 J. Wang, G. Cao, R. Duan, X. Li and X. Li, *Acta Phys.-Chim. Sin.*, 2023, **39**, 2212005.
16 E. Abd-Alkuder Salman, K. Abaid Samawi, M. Fawzi Nassar, G. Abdulkareem-Alsultan and E. Abdulmalek, *J. Electroanal. Chem.*, 2023, **945**, 117629.
17 A. G. Alsultan, N. Asikin-Mijan, L. K. Obeas, A. Islam, N. Mansir, S. H. Teo, S. Z. Razali, M. F. Nassar, S. Mohamad and Y. H. Taufiq-Yap, *Catalysts*, 2022, **12**, 566.
18 J. L. Shi, C. Tang, H. J. Peng, L. Zhu, X. B. Cheng, J. Q. Huang, W. Zhu and Q. Zhang, *Small*, 2015, **11**, 5243–5252.
19 J. Wang, C. Fu, X. Wang, Y. Yao, M. Sun, L. Wang and T. Liu, *Electrochim. Acta*, 2018, **292**, 568–574.
20 X. Chen, Z. Zhu, E. Vargun, Y. Li, P. Saha and Q. Cheng, *J. Electroanal. Chem.*, 2023, **928**, 117046.
21 B. Li, A. H. Amin, A. M. Ali, M. Isam, A. A. Lagum, M. M. Sabugaa, R. D. Pecho, H. M. Salman and M. F. Nassar, *Chemosphere*, 2023, **13**, 139208.
22 W. Yao, W. Zheng, K. Han and S. Xiao, *J. Mater. Chem. A*, 2020, **8**, 19028–19042.
23 S. Chen, Z. Wu, J. Luo, X. Han, J. Wang, Q. Deng, Z. Zeng and S. Deng, *Electrochim. Acta*, 2019, **312**, 109–118.
24 B. Chen, Z. Zhang, S. Kim, S. Lee, J. Lee, W. Kim and K. Yong, *ACS Appl. Mater. Interfaces*, 2018, **10**, 44518–44526.
25 A. Hassan, K. A. Samawi, M. F. Nassar, R. Haddad, A. Roostaie and S. M. Sadeghzadeh, *Catal. Lett.*, 2023, **153**, 2900–2909.
26 F. Song and X. Hu, *Nat. Commun.*, 2014, **5**, 4477.
27 F. Ning, M. Shao, C. Zhang, S. Xu, M. Wei and X. Duan, *Nano Energy*, 2014, **7**, 134–142.
28 M.-Q. Zhao, Q. Zhang, J.-Q. Huang, G.-L. Tian, J.-Q. Nie, H.-J. Peng and F. Wei, *Nat. Commun.*, 2014, **5**, 3410.
29 J. Zhang, Z. Li, Y. Chen, S. Gao and X. W. D. Lou, *Angew. Chem., Int. Ed.*, 2018, **57**, 10944–10948.
30 L. Zhang, Z. Chen, N. Dongfang, M. Li, C. Diao, Q. Wu, X. Chi, P. Jiang, Z. Zhao and L. Dong, *Adv. Energy Mater.*, 2018, **8**, 1802431.
31 M. Faraji, F. Parsaee and M. Kheirmand, *J. Solid State Chem.*, 2021, **303**, 122529.
32 S. Chen, L. Zhao, W. Wei, Y. Li and L. Mi, *J. Alloys Compd.*, 2020, **831**, 154794.
33 H. Huang, C. Yu, H. Huang, W. Guo, M. Zhang, X. Han, Q. Wei, S. Cui, X. Tan and J. Qiu, *Small Methods*, 2019, **3**, 1900259.
34 M. T. Dejpasand, S. Sharifi, E. Saievar-Iranizad, A. Yazdani and K. Rahimi, *J. Energy Storage*, 2021, **42**, 103103.
35 M. Faraji and S. Moradi Dehaghi, *Inorg. Chem. Commun.*, 2021, **123**, 108328.
36 X. Guan, M. Huang, L. Yang, G. Wang and X. Guan, *Chem. Eng. J.*, 2019, **372**, 151–162.
37 C. Sun, J. Yang, X. Rui, W. Zhang, Q. Yan, P. Chen, F. Huo, W. Huang and X. Dong, *J. Mater. Chem. A*, 2015, **3**, 8483–8488.
38 Z. Jiang, Z. Li, Z. Qin, H. Sun, X. Jiao and D. Chen, *Nanoscale*, 2013, **5**, 11770–11775.
39 G. Yilmaz, K. M. Yam, C. Zhang, H. J. Fan and G. W. Ho, *Adv. Mater.*, 2017, **29**, 1606814.
40 S. H. Kazemi, B. Hosseinzadeh, H. Kazemi, M. A. Kiani and S. Hajati, *ACS Appl. Mater. Interfaces*, 2018, **10**, 23063–23073.
41 G. Wang, X. Shen, B. Wang, J. Yao and J. Park, *Carbon*, 2009, **47**, 1359–1364.
42 S. Jin, Y. Feng, J. Jia, F. Zhao, Z. Wu, P. Long, F. Li, H. Yu, C. Yang, Q. Liu, B. Zhang, H. Song and W. Feng, *Energy Environ. Mater.*, 2023, **6**, e12373.
43 M. Faraji, P. Derakhshi, K. Tahvildari and Z. Yousefian, *Solid State Sci.*, 2018, **83**, 152–160.
44 F. Lai, Y. E. Miao, L. Zuo, H. Lu, Y. Huang and T. Liu, *Small*, 2016, **12**, 3235–3244.
45 F. Cao, M. Zhao, Y. Yu, B. Chen, Y. Huang, J. Yang, X. Cao, Q. Lu, X. Zhang and Z. Zhang, *J. Am. Chem. Soc.*, 2016, **138**, 6924–6927.
46 Z. Ye, F. Wang, C. Jia, K. Mu, M. Yu, Y. Lv and Z. Shao, *Chem. Eng. J.*, 2017, **330**, 1166–1173.
47 J. Wu, Y. Gong, Q. Fu and C. Pan, *MRS Adv.*, 2019, **4**, 1887–1893.
48 K. Li, M. Liu, S. Li, F. Huang, L. Wang and H. Zhang, *J. Alloys Compd.*, 2020, **817**, 152712.
49 D. Zhang, X. Guo, X. Tong, Y. Chen, M. Duan, J. Shi, C. Jiang, L. Hu, Q. Kong and J. Zhang, *J. Alloys Compd.*, 2020, **837**, 155529.
50 Q. Pang, J. Tang, H. Huang, X. Liang, C. Hart, K. C. Tam and L. F. Nazar, *Adv. Mater.*, 2015, **27**, 6021–6028.
51 X. Liang, Y. Rangom, C. Y. Kwok, Q. Pang and L. F. Nazar, *Adv. Mater.*, 2017, **29**, 1603040.
52 X. Liang, C. Hart, Q. Pang, A. Garsuch, T. Weiss and L. F. Nazar, *Nat. Commun.*, 2015, **6**, 5682.
53 Q. Lin, L. Huang, W. Liu, Z. Li, R. Fang, D.-W. Wang, Q.-H. Yang and W. Lv, *Phys. Chem. Chem. Phys.*, 2021, **23**, 21385–21398.
54 F. Y. Fan, W. C. Carter and Y. M. Chiang, *Adv. Mater.*, 2015, **27**, 5203–5209.
55 Z. Sun, J. Zhang, L. Yin, G. Hu, R. Fang, H.-M. Cheng and F. Li, *Nat. Commun.*, 2017, **8**, 14627.
56 M. Li, S. Ji, X. Ma, H. Wang, X. Wang, V. Linkov and R. Wang, *ACS Appl. Mater. Interfaces*, 2022, **14**, 16310–16319.
57 Q. Zhang, Y. Wang, Z. W. Seh, Z. Fu, R. Zhang and Y. Cui, *Nano Lett.*, 2015, **15**, 3780–3786.

58 D. Wei, Y. Liu, Y. Wang, H. Zhang, L. Huang and G. Yu, *Nano Lett.*, 2009, **9**, 1752–1758.
59 C. Ma, Q. Liao, H. Sun, S. Lei, Y. Zheng, R. Yin, A. Zhao, Q. Li and B. Wang, *Nano Lett.*, 2018, **18**, 386–394.
60 S. Chen, Y. Xu, C. Li, X. Xiao and Y. Chen, *Sol. Energy*, 2018, **174**, 66–72.
61 L. Paramanik, S. Sultana and K. M. Parida, *J. Colloid Interface Sci.*, 2022, **625**, 83–99.

